

# CHASE: 3D-Consistent Human Avatars with Sparse Inputs via Gaussian Splatting and Contrastive Learning

Haoyu Zhao<sup>\*1,2</sup>, Hao Wang<sup>\*3</sup>, Chen Yang<sup>\*1</sup>, Wei Shen<sup>†1</sup>

<sup>1</sup>MoE Key Lab of Artificial Intelligence, AI Institute, Shanghai Jiao Tong University

<sup>2</sup>School of Computer Science, Wuhan University,

<sup>3</sup>Wuhan National Laboratory for Optoelectronics, Huazhong University of Science and Technology, haoyu.zhao@whu.edu.cn, ycyangchen@sjtu.edu.cn, wanghao020110@hust.edu.cn, wei.shen@sjtu.edu.cn

## Abstract

Recent advancements in human avatar synthesis have utilized radiance fields to reconstruct photo-realistic animatable human avatars. However, both NeRFs-based and 3DGS-based methods struggle with maintaining 3D consistency and exhibit suboptimal detail reconstruction, especially with sparse inputs. To address this challenge, we propose **CHASE**, which introduces supervision from intrinsic 3D consistency across poses and 3D geometry contrastive learning, achieving performance comparable with sparse inputs to that with full inputs. Following previous work, we first integrate a skeleton-driven rigid deformation and a non-rigid cloth dynamics deformation to coordinate the movements of individual Gaussians during animation, reconstructing basic avatar with coarse 3D consistency. To improve 3D consistency under sparse inputs, we design Dynamic Avatar Adjustment(DAA) to adjust deformed Gaussians based on a selected similar pose/image from the dataset. Minimizing the difference between the image rendered by adjusted Gaussians and the image with the similar pose serves as an additional form of supervision for avatar. Furthermore, we propose a 3D geometry contrastive learning strategy to maintain the 3D global consistency of generated avatars. Though **CHASE** is designed for sparse inputs, it surprisingly outperforms current SOTA methods **in both full and sparse settings** on the ZJU-MoCap and H36M datasets, demonstrating that our **CHASE** successfully maintains avatar’s 3D consistency, hence improving rendering quality. The code will be made available.

## Introduction

Photorealistic rendering and animation of human bodies is a crucial research area with wide-ranging applications in AR/VR, visual effects, visual try-on, and movie production (Zackariasson and Wilson 2012; Healey, Wang, and et al 2021). Early works (Mildenhall et al. 2021; Oechsle, Peng, and Geiger 2021; Niemeyer et al. 2020; Peng et al. 2021b; Wang et al. 2022a; Sitzmann et al. 2021) for creating human avatars relied on capturing high-quality data through multi-camera setups, which is extensive computing and needs lots

of manual effort. While these methods excel at creating a single scene/object from sufficient input views, it is very challenging for them to generalize to new scenes/objects with few samples (Kwon et al. 2024).

Recent advancements have explored using neural radiance fields (NeRF) for modeling 3D human avatars (Mildenhall et al. 2021; Wang et al. 2022a), typically employing parametric body models to model deformations. Some methods (Chen et al. 2022; Zhao et al. 2022) use human template models to facilitate generalizable and robust synthesis. Though NeRF-based methods have made significant progress in generalizable human rendering, they are less efficient to train and render due to their computationally intensive per-pixel volume rendering process.

Point-based rendering (Zheng et al. 2023) has emerged as an efficient alternative to NeRFs, offering significantly faster rendering. The recently proposed 3D Gaussian Splatting (3DGS) (Kerbl et al. 2023) gains popularity for its efficient rasterization-based rendering speed. Numerous works have further explored the 3D Gaussian representation for dynamic 3D human avatars (Lei et al. 2024; Moreau et al. 2024; Shao et al. 2024; Hu et al. 2024b; Kocabas et al. 2024; Wang et al. 2024a; Qian et al. 2024; Hu et al. 2024a). However, these methods often face challenges in maintaining 3D consistency and producing high-quality reconstructions, particularly with sparse inputs.

To address the aforementioned issues, we propose **CHASE**, which is capable of reconstructing 3D Consistent Human Avatars with Sparse inputs via Gaussian Splatting and contrastivE learning. We first integrates a skeleton-driven rigid deformation, and a non-rigid cloth dynamics deformation to create human avatar with coarse 3D consistency. To enhance 3D consistency under sparse inputs, we utilize the intrinsic 3D consistency of images across different poses within the same person. Specifically, for each training pose/image, we select a similar pose/image from the dataset and then adjust the deformed Gaussians using the proposed Dynamic Avatar Adjustment (DAA), an explicit point-based control graph adjustment strategy, to the selected similar pose. Then we minimize differences between the rendered image of the adjusted Gaussians and the image corresponding to the selected similar pose, which serves as an additional form of supervision for human avatar. Additionally, we employ 3D geometry contrastive learn-

Copyright © 2025, Association for the Advancement of Artificial Intelligence (www.aaai.org). All rights reserved.

<sup>\*</sup>Equal contributions.

<sup>†</sup>Corresponding Author.

Haoyu Zhao completed this work during an internship at Shanghai Jiao Tong University.

ing, utilizing features from a 3D feature extractor, to further enhance the global 3D consistency of generated human avatars. We conduct extensive experiments on the ZJU-MoCap data (Peng et al. 2021c), H36M (Ionescu et al. 2013) and find that **CHASE not only achieves better performance in sparse inputs setting but also outperforms other SOTAs in full setting.**

In summary, our work makes the following contributions:

- We propose an explicit point-based control graph adjustment strategy, which introduces a novel 2D image supervision to 3D human body modeling, enhancing the 3D consistency of human avatars.
- We propose 3D geometry contrastive learning to enforce consistency across different representations of the same pose and facilitate effective 3D global understanding.
- Extensive experiments show that our **CHASE** achieves SOTA performance quantitatively and qualitatively under full and sparse settings.

## Related Work

### Contrastive Representation Learning

Contrastive Representation Learning is one of the mainstream self-supervised learning paradigms (Hadsell, Chopra, and LeCun 2006), which learns potential semantics from constructed invariance or equivariance (Rumen et al. 2022). In 3D, PointContrast (Xie et al. 2020) proposes geometric augmentation to generate positive and negative pairs. CrossPoint (Afham et al. 2022) uses both inter- and intra-modal contrastive learning. PointCLIP (Zhang et al. 2022) achieves image-point alignment by projecting point clouds onto 2D depth images. RECON (Qi et al. 2023) focuses on single- and cross-modal contrastive learning through discriminative contrast (Khosla et al. 2020) or global feature alignment (Radford et al. 2021). Our **CHASE** introduces a 3D geometry contrastive learning method across different poses to enforce consistency across different representations of the same pose.

### 3D Editing and Deformation

Traditional deformation methods in computer graphics are typically based on Laplacian coordinates (Gao et al. 2019; Sorkine and Alexa 2007; Sorkine 2005), Poisson equations (Yu et al. 2004), and cage-based methods (Yifan et al. 2020). However, these methods often rely on implicit and computationally expensive NeRF-based approaches.

Numerous works (Chen et al. 2024; Wang et al. 2024b) have proposed techniques for editing 3D Gaussian Splatting (3DGS)(Kerbl et al. 2023). SuGaR(Guédon and Lepetit 2024) introduces a mesh extraction method that produces meshes from 3DGS, which can then be edited. SC-GS (Huang et al. 2024) proposes deforming Gaussians by transferring the movement of control points. Our **CHASE** employs a novel explicit point-based control graph deformation strategy, which is more intuitive and efficient.

### 3D Human Modeling

Since the high-quality rendering achieved by the seminal work Neural Radiance Fields (NeRF)(Mildenhall et al.

2021), there has been a surge of research on neural rendering for human avatars(Liu et al. 2021; Li et al. 2023; Peng et al. 2021c). Although NeRF is designed for static objects, HumanNeRF (Weng et al. 2022) extends NeRF to enable capturing dynamic human motion using just a single monocular video. Neural Body (Peng et al. 2021c) associates a latent code with each SMPL (Loper et al. 2015) vertex to encode appearance, which is then transformed into observation space based on the human pose. Furthermore, Neural Actor (Liu et al. 2021) learns a deformable radiance field with SMPL (Loper et al. 2015) as guidance and utilizes a texture map to improve the final rendering quality. Posevocab (Li et al. 2023) designs joint-structured pose embeddings to encode dynamic appearances under different key poses, allowing for more effective learning of joint-related appearances. However, a major limitation of NeRF-based methods is that NeRFs are slow to train and render.

Point-based rendering (Zheng et al. 2023) has proven to be an efficient alternative to NeRFs for fast inference and training. Extending point clouds to 3D Gaussians, 3D Gaussian Splatting (3DGS)(Kerbl et al. 2023) models the rendering process by splatting a set of 3D Gaussians onto the image plane via alpha blending. Given the impressive performance of 3DGS in both quality and speed, numerous works have further explored the 3D Gaussian representation for dynamic 3D human avatar reconstruction(Lei et al. 2024; Qian et al. 2024; Hu et al. 2024b; Kocabas et al. 2024). Human Gaussian Splatting (Moreau et al. 2024) showcases 3DGS as an efficient alternative to NeRF. SplattingAvatar (Shao et al. 2024) and GomAvatar (Wen et al. 2024) extend lifted optimization to simultaneously optimize the parameters of the Gaussians while walking on the triangle mesh. However, these methods struggle to maintain 3D consistency and produce low-quality reconstructions when applied to human avatar creation with only sparse inputs. Our **CHASE** introduces a novel 2D image supervision to 3D human body modeling and 3D geometry contrastive learning, enhancing the 3D consistency of human avatars.

## Preliminaries

**SMPL (Loper et al. 2015).** The SMPL model is a pre-trained parametric human model representing body shape and pose. In SMPL, body shape and pose are controlled by pose and shape. In this work, we apply the Linear Blend Skinning (LBS) algorithm used in SMPL to transform points from a canonical space to a posed space.

**LBS (Sumner, Schmid, and Pauly 2007).** Linear Blend Skinning (LBS) is a weight-based technique that associates each vertex with one or more joints and uses weight values to describe the influence of each joint on the vertex. Vertex deformation is calculated by linearly interpolating transformations on the associated joints:  $\mathcal{X}'_v = \sum_{j=1}^J w_j(\mathcal{X}_v)B_j\mathcal{X}_v$ , where  $J$  represents the number of joints,  $N$  represents the number of vertices,  $\mathcal{X}'_v \in \mathbb{R}^{N \times 3}$  is the new position of the skinned vertex,  $w \in \mathbb{R}^{N \times J}$  is the skinning weight matrix,  $B \in \mathbb{R}^{J \times 4 \times 4}$  is the affine transformation matrix of each

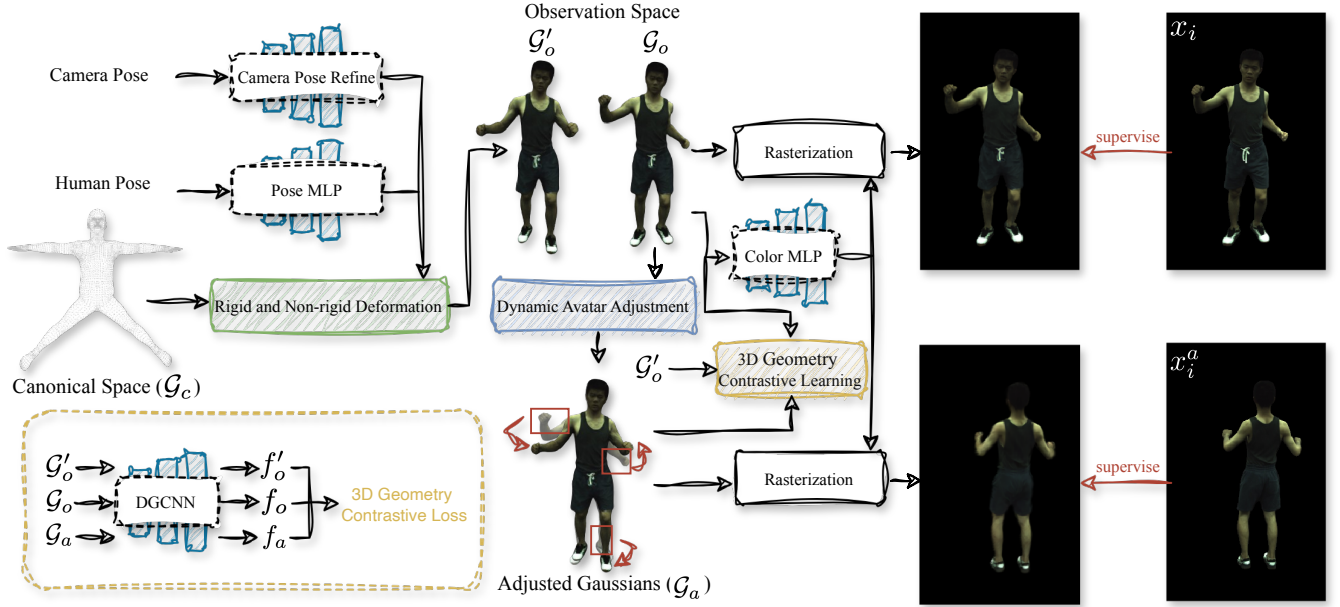


Figure 1: **CHASE Framework.** We first initialize 3D Gaussians in canonical space by randomly sampling 50k points on the SMPL mesh surface. Then, we integrate a rigid human articulation and a non-rigid deformation neural field to deform the 3D Gaussians in canonical space  $\mathcal{G}_c$  to the observation space  $\mathcal{G}_o$ . Next, we select similar poses/images from the dataset for each training pose/image and then adjust the deformed Gaussians  $\mathcal{G}_o$  to the similar pose  $\mathcal{G}_a$  using Dynamic Avatar Adjustment (DAA). Minimizing the differences between the rendered adjusted Gaussians  $\mathcal{G}_a$  and the selected similar images  $x_i^a$  serves as an additional supervision. Furthermore, we propose a 3D geometry contrastive learning, which involves comparing features from a 3D feature extractor to improve the avatar’s global 3D consistency. Negative pairs consist of the features of the deformed Gaussians  $\mathcal{G}_o$  and the adjusted Gaussians  $\mathcal{G}_a$ . In contrast, positive pairs include the features of  $\mathcal{G}'_o$ , which is deformed from the canonical space to match the pose adjustments seen in  $\mathcal{G}_a$ , and  $\mathcal{G}_a$ .

joint representing rotation and translation, (i.e. bone transforms) and  $\mathcal{X}_v \in \mathbb{R}^{N \times 3}$  is the original mesh vertex position.

**3D Gaussian Splatting (3DGS) (Kerbl et al. 2023).** 3DGS explicitly represents scenes using point clouds, where each point is modeled as a 3D Gaussian defined by a covariance matrix  $\Sigma$  and a center point  $\mathcal{X}$ , the latter referred to as the mean. The value at point  $\mathcal{X}$  is:

$$G(\mathcal{X}) = e^{-\frac{1}{2}\mathcal{X}^T \Sigma^{-1} \mathcal{X}}. \quad (1)$$

For differentiable optimization, the covariance matrix  $\Sigma$  is decomposed into a scaling matrix  $\mathcal{S}$  and a rotation matrix  $\mathcal{R}$ , such that  $\Sigma = \mathcal{R}\mathcal{S}\mathcal{S}^T\mathcal{R}^T$ .  $\mathcal{S}$  and  $\mathcal{R}$  are stored as the diagonal vector  $s \in \mathbb{R}^{N \times 3}$  and a quaternion vector  $r \in \mathbb{R}^{N \times 4}$ , respectively.

In rendering novel views, differential splatting as introduced by (Yifan et al. 2019), involves using a viewing transform  $W$  and the Jacobian matrix  $J$  of the affine approximation of the projective transformation to compute the transformed covariance matrix:  $\Sigma' = JW\Sigma W^T J^T$ . The color and opacity at each pixel are computed from the Gaussian’s representations:  $G(\mathcal{X}) = e^{-\frac{1}{2}\mathcal{X}^T \Sigma^{-1} \mathcal{X}}$ . The blending of  $N$

ordered points overlapping a pixel is given by the formula:

$$\mathcal{C} = \sum_{i \in N} c_i \alpha_i \prod_{j=1}^{i-1} (1 - \alpha_j), \quad (2)$$

where  $c_i$ ,  $\alpha_i$  represent the density and color of this point computed by a 3D Gaussian  $G$  with covariance  $\Sigma$  multiplied by an optimizable per-point opacity and SH color coefficients.

## Method

We illustrate the pipeline of our **CHASE** in Fig. 1. The inputs include images  $X = \{x_i\}_{i=1}^N$  obtained from monocular videos, fitted SMPL parameters  $P = \{p_i\}_{i=1}^N$ , and foreground masks  $M = \{m_i\}_{i=1}^N$  of images. **CHASE** optimizes 3D Gaussians in canonical space, which are then deformed to match the observation space and be rendered with a given camera view.

### Non-rigid and Rigid Deformation

Inspired by (Weng et al. 2022; Qian et al. 2024), we deform 3D Gaussians from canonical space  $\mathcal{G}_c$  to observation space  $\mathcal{G}_o$  by integrating a rigid articulation with a non-rigid transformation. We employ a non-rigid deformation network

that takes the canonical positions  $\mathcal{X}_c$  of the 3D Gaussians  $\mathcal{G}_c$  and a pose latent code which encodes SMPL pose  $p_i$  using a lightweight hierarchical pose encoder (Mihajlovic et al. 2021) as input. The network then outputs the offsets for various parameters of the 3D Gaussians  $\mathcal{G}_c$ :  $\Delta(\mathcal{X}, \mathcal{C}, \alpha, s, r)$ . The canonical Gaussians are deformed by:

$$\mathcal{X}_d = \mathcal{X}_c + \Delta\mathcal{X}, \mathcal{C}_d = \mathcal{C}_c + \Delta\mathcal{C}, \quad (3)$$

$$\alpha_d = \alpha_c + \Delta\alpha, s_d = s_c \cdot \exp(\Delta s), \quad (4)$$

$$r_d = r_c \cdot [1, \Delta r_1, \Delta r_2, \Delta r_3], \quad (5)$$

where quaternion multiplication  $\cdot$  corresponds to multiplying the rotation matrices. With  $[1, 0, 0, 0]$  as the identity rotation,  $r_d = r_c$  when  $\delta r = \mathbf{0}$ , thus keeping the original orientation.

We further apply a LBS-based rigid transformation to map the non-rigidly deformed 3D Gaussians  $\mathcal{G}_d$  to the observation space  $\mathcal{G}_o$ . This transformation utilizes LBS weights predicted by a Skinning MLP  $f_{\theta_r}$ . This process aligns the Gaussians with the target pose in  $\mathcal{G}_o$ :

$$T = \sum_{j=1}^J f_{\theta_r}(\mathcal{X}_d)_j B_j, \mathcal{X}_o = T\mathcal{X}_d, \quad (6)$$

$$\mathcal{R}_o = T_{1:3,1:3}\mathcal{R}_d, \quad (7)$$

where  $\mathcal{R}$  is the matrix representations of rotation.

### Dynamic Avatar Adjustment

To address extremely sparse inputs, we leverage the intrinsic 3D consistency of human avatars across different poses/images, as shown in Fig. 2. Specifically, for each training pose/image, we select a similar pose  $p_i^a$  with its paired image  $x_i^a$  from the dataset and then use a dense motion field  $F_{adj}$  as an additional adjustment to transform deformed Gaussians  $\mathcal{G}_o$  into adjusted Gaussians  $\mathcal{G}_a$ , aligning them with the selected pose/image ( $p_i^a/x_i^a$ ). In this way, we successfully introduce an additional 2D image supervision, improving the 3D consistency of human avatars.

To achieve precise control of the 3D Gaussians, we sample 6,890 points from the SMPL model (Loper et al. 2015) as our sparse control points in canonical space. Then, we obtain the dense motion field using LBS by locally inheriting the LBS weights from neighboring control points. Specifically, for each 3D Gaussian, we use the k-nearest neighbor (KNN) search to find its nearest neighboring control points in canonical space. The entire adjustment process is as:

$$w = w_{smpl}[\text{KNN}(xyz_{cano}, xyz_{smpl})], \quad (8)$$

$$T_o = \sum_{j=1}^J w_j B_{oj}, T'_o = \sum_{j=1}^J w_j B'_{oj}. \quad (9)$$

Here,  $w_{smpl}$  denotes the LBS weights of the sparse control points, and  $T_o(B_o)$  and  $T'_o(B'_o)$  represent the rigid transformations (bone transformations) from canonical space  $\mathcal{G}_c$  to deformed Gaussians  $\mathcal{G}_o$ , and to the Gaussians with the selected similar pose  $\mathcal{G}'_o$ , respectively. We then obtain  $F_{adj}$ , which transforms the deformed Gaussians  $\mathcal{G}_o$  into adjusted Gaussians  $\mathcal{G}_a$ , aligning them with the selected pose  $p_i^a$  as:

$$F_{adj} = F_o F_o^{-1}. \quad (10)$$

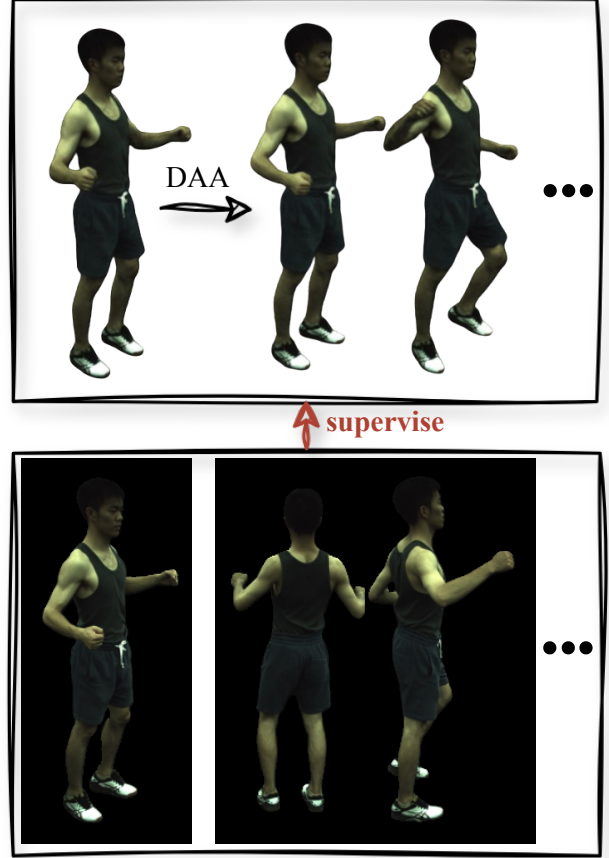


Figure 2: For each training pose/image, we select similar poses/images from the dataset and then adjust the deformed Gaussians using Dynamic Avatar Adjustment (DAA). By minimizing the discrepancy between the rendered image of the adjusted avatar and the selected similar pose image, we introduce an additional supervision, thereby enhancing the creation of animatable avatars.

We adjust the deformed Gaussians  $\mathcal{G}_o$  to adjusted Gaussians  $\mathcal{G}_a$  by adjusting its position and rotation as follow:

$$\mathcal{X}_a = F_{adj}\mathcal{X}_o, \quad (11)$$

$$\mathcal{R}_a = F_{adj1:3,1:3}\mathcal{R}_o. \quad (12)$$

### 3D Geometry Contrastive learning

Inspired by the success of contrastive learning in image processing and static point cloud analysis, we advocate for adopting 3D geometry contrastive learning to ensure 3D consistency during animation. To this end, we treat the 3D Gaussians as a 3D point cloud and use DGCNN (Wang et al. 2019) as the feature extractor. The point cloud feature extractor processes the positions of the 3D Gaussians in the observation space  $\mathcal{G}_o$ , the adjusted Gaussians  $\mathcal{G}_a$ , and  $\mathcal{G}'_o$ , which is deformed from the canonical space to match the selected pose  $p_i^a$ , and outputs their features, creating inter-

mediate graph features to capture global geometric information better. The feature vectors are projected into an invariant space. We denote the projected features of  $\mathcal{G}_o$ ,  $\mathcal{G}_a$ , and  $\mathcal{G}'_o$  as  $f_o$ ,  $f_a$ , and  $f'_o$ , respectively.

In the invariant space, we aim to maximize the similarity between  $f_a$  and  $f'_o$ , denoted as  $D_{positive}$ , and minimize the similarity between  $f_a$  and  $f_o$ , denoted as  $D_{negative}$ . Therefore, we compute the 3D geometry contrastive loss  $\mathcal{L}_{contrastive}$  as:

$$D_{positive} = \|f_a - f'_o\|_2, \quad (13)$$

$$D_{negative} = \|f_a - f_o\|_2, \quad (14)$$

$$\mathcal{L}_{contrastive} = \max(0, D_{positive} - D_{negative}). \quad (15)$$

## Optimization

**Color MLP.** Following (Qian et al. 2024), we use the inverse rigid transformation to canonicalize the viewing direction:  $\hat{d} = T_{1:3,1:3}^{-1}d$ , where  $T$  and  $d$  is the forward transformation matrix defined in LBS and viewing direction, respectively. Theoretically, canonicalizing viewing direction also promotes consistency of the specular component of canonical 3D Gaussians under rigid transformations.

**Pose correction.** Following (Qian et al. 2024), SMPL (Loper et al. 2015) parameter fittings from images can be inaccurate. We additionally optimize the per-sequence shape parameter and per-frame translation, global rotation, and local joint rotations.

**Loss function.** Our full loss function consists of several components: an RGB loss  $\mathcal{L}_{rgb}$ , a mask loss  $\mathcal{L}_{mask}$ , and a perceptual similarity (LPIPS) loss  $\mathcal{L}_{LPIPS}$ . We compute these losses on both images rendered from the deformed Gaussians  $\mathcal{G}_o$  and the adjusted Gaussians  $\mathcal{G}_a$  with their corresponding ground truth images. Additionally, we include a skinning weight regularization loss  $\mathcal{L}_{skin}$ , as well as isometric regularization losses for both position and covariance,  $\mathcal{L}_{isopos}$  and  $\mathcal{L}_{isocov}$ , respectively, following (Qian et al. 2024). We also incorporate a 3D geometry contrastive loss  $\mathcal{L}_{contrastive}$ :

$$\mathcal{L} = \mathcal{L}_{rgb} + \lambda_1 \mathcal{L}_{mask} + \lambda_2 \mathcal{L}_{LPIPS} + \lambda_3 \mathcal{L}_{skin} + \lambda_4 \mathcal{L}_{isopos} + \lambda_5 \mathcal{L}_{isocov} + \lambda_6 \mathcal{L}_{contrastive}, \quad (16)$$

where  $\lambda$ 's are loss weights. For further details of the loss definition and respective weights, please refer to the Supp.Mat.

## Experiment

### Dataset

**ZJU-MoCap (Peng et al. 2021c).** This dataset features multiple-view videos captured by 21 cameras, with human poses recorded using a marker-less motion capture system. For our experiments, we selected six sequences (377, 386, 387, 392, 393, 394). Following the protocol established by HumanNeRF (Weng et al. 2022) and 3DGS-Avatar (Qian et al. 2024), we use a single camera for training and the remaining cameras for evaluation. The foreground masks, camera, and SMPL parameters provided by the data set are

Table 1: **Quantitative Results on ZJU-MoCap (Peng et al. 2021c).** CHASE achieves state-of-the-art performance across every method. The **best** and the **second best** results are denoted by pink and yellow. Frames per second (FPS) is measured on an RTX 3090. We train our model on the dataset that includes only 5% of the origin data for fair quantitative comparison. The metrics are reported in the last four rows of the table.  $LPIPS^\dagger = LPIPS \times 1000$ .

Method:	PSNR $\uparrow$	SSIM $\uparrow$	LPIPS $\dagger$ $\downarrow$	FPS
NeuralBody (Peng et al. 2021c)	29.07	0.962	52.29	1.5
Ani-NeRF (Peng et al. 2021a)	29.17	0.961	51.98	1.1
HumanNeRF (Weng et al. 2022)	30.24	0.968	31.73	0.3
MonoHuman (Yu et al. 2023)	29.38	0.964	37.51	0.1
3DGS-Avatar (Qian et al. 2024)	30.62	0.965	<b>30.28</b>	50
GauHuman (Hu et al. 2024b)	<b>30.79</b>	0.960	32.73	180
GoMAvatar (Wen et al. 2024)	<b>30.37</b>	<b>0.969</b>	32.53	43
Ours	<b>30.81</b>	<b>0.970</b>	27.48	50
3DGS-Avatar* (Qian et al. 2024)	29.98	0.957	40.01	50
GauHuman* (Hu et al. 2024b)	<b>30.35</b>	0.957	<b>35.68</b>	180
GoMAvatar* (Wen et al. 2024)	30.01	<b>0.958</b>	42.88	43
Ours*	<b>30.48</b>	<b>0.969</b>	29.94	50

Table 2: **Quantitative Results on H36M (Ionescu et al. 2013).** Our CHASE outperforms current SOTA methods in both full and sparse settings

Method:	Training Poses		Novel Poses	
	PSNR $\uparrow$	SSIM $\uparrow$	PSNR $\uparrow$	SSIM $\uparrow$
NARF (Noguchi et al. 2021)	23.00	0.898	22.27	0.881
NeuralBody (Peng et al. 2021c)	22.89	0.896	23.09	0.891
Ani-NeRF (Peng et al. 2021a)	23.00	0.890	22.55	0.880
ARAH (Wang et al. 2022b)	24.79	0.918	23.42	0.896
3DGS-Avatar (Qian et al. 2024)	<b>32.89</b>	<b>0.982</b>	<b>32.50</b>	<b>0.983</b>
Ours	<b>33.29</b>	<b>0.984</b>	<b>32.93</b>	<b>0.982</b>
3DGS-Avatar* (Qian et al. 2024)	<b>32.48</b>	<b>0.976</b>	<b>32.17</b>	<b>0.981</b>
Ours*	<b>32.91</b>	<b>0.983</b>	<b>32.64</b>	<b>0.982</b>

used for evaluation purposes. **We use 5% of the dataset to simulate sparse inputs.**

**H36M (Ionescu et al. 2013).** H36M is another widely used dataset for human avatar research, comprising multi-view videos from four cameras and human poses captured via a marker-based motion capture system. It features multiple subjects performing a variety of complex actions. We conducted experiments on sequences from subjects S1, S5, S6, S7, S8, S9, and S11, selecting representative actions and dividing the videos into training and test frames. Adhering to the protocol set by ARAH (Wang et al. 2022b), we use three cameras, [54138969, 55011271, 58860488], for training and the remaining camera, [60457274], for testing, and follow their preprocessing steps. We use the SMPL parameters and foreground humans following (Peng et al. 2021a).

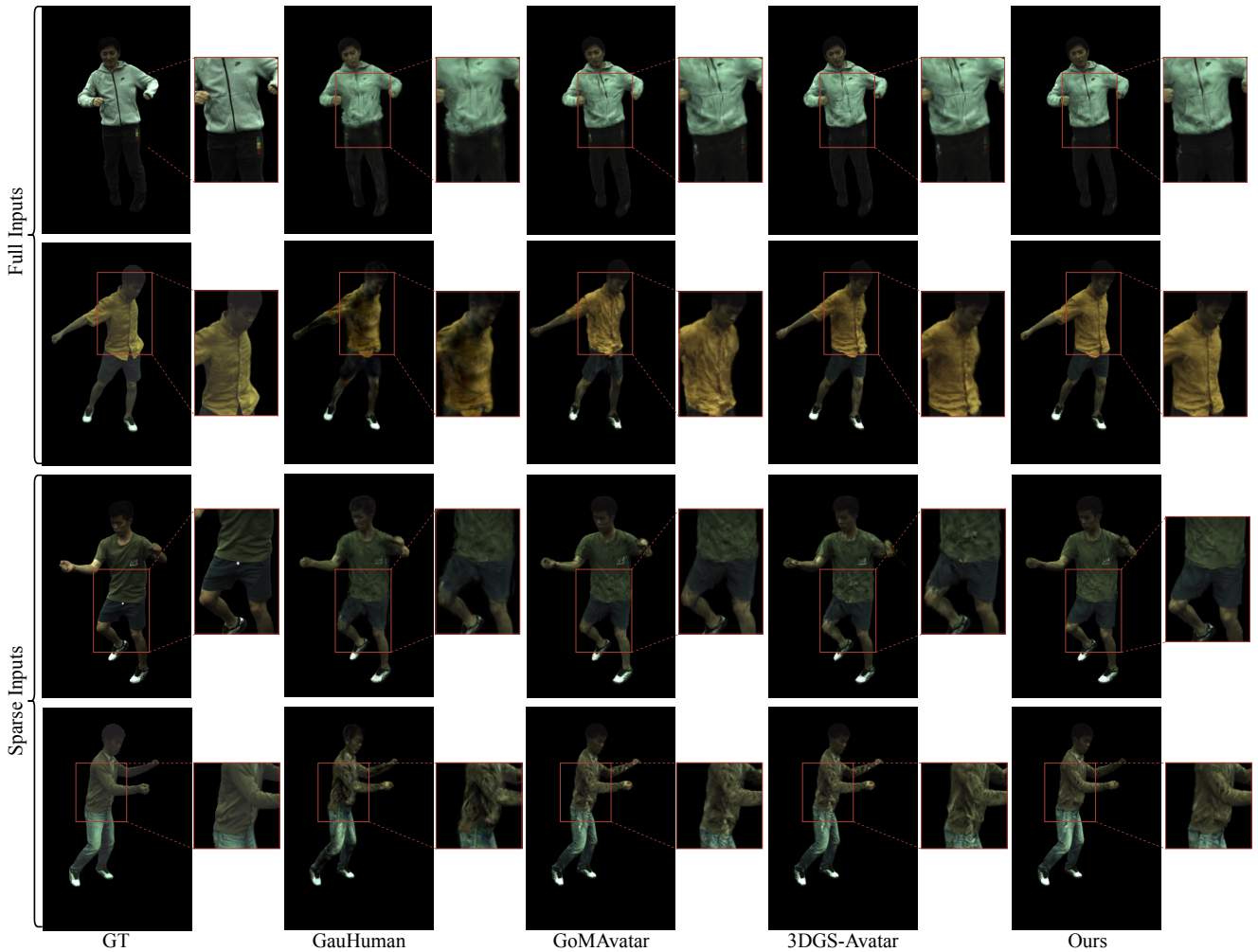


Figure 3: **Qualitative Comparison on ZJU-MoCap (Peng et al. 2021c).** We present results for full and sparse inputs (5% of the full inputs) on the ZJU-MoCap dataset. Results show that our **CHASE** can produce realistic details with both full and sparse inputs, while other approaches struggle to generate smooth details.

### Comparison with State-of-the-art Methods

We compare our **CHASE** with various SOTA methods for human avatars, including NerF-based methods such as NeuralBody (Peng et al. 2021c), Ani-NeRF (Peng et al. 2021a), HumanNeRF (Weng et al. 2022), and MonoHuman (Yu et al. 2023), and 3DGS-based methods such as 3DGS-Avatar (Qian et al. 2024), GauHuman (Hu et al. 2024b), and GoMAvatar (Wen et al. 2024) under monocular setup on ZJU-MoCap (Peng et al. 2021c). The quantitative results are shown in Tab. 1. Overall, our proposed **CHASE** achieves the best performance in terms of PSNR, SSIM, and LPIPS with both full and sparse inputs. Our **CHASE** shows only a small performance drop when using only 5% of the data and significantly outperforms SOTA methods on LPIPS. It is evidence that our method successfully maintains 3D consistency even with sparse inputs.

Qualitative comparisons on novel view synthesis are shown in Fig. 3. We observe that our method preserves more

details compared to other SOTA methods. They often struggle to maintain 3D consistency and deliver suboptimal detail reconstruction in human avatar modeling, particularly when only sparse inputs are available.

For H36M (Ionescu et al. 2013), we report the quantitative results against NerF-based methods such as NARF (Noguchi et al. 2021), NeuralBody (Peng et al. 2021c), Ani-NeRF (Peng et al. 2021a) and ARAH (Wang et al. 2022b), and 3DGS-based methods such as 3DGS-Avatar (Qian et al. 2024) in Tab. 2. Our **CHASE** significantly outperforms these methods with sparse inputs, showing that our **CHASE** generalizes well to novel poses with sparse inputs and reconstructs human avatars with better appearance and geometry detail. For qualitative comparisons on novel pose synthesis, please refer to the Supp.Mat.

Table 3: **Ablation Study on ZJU-MoCap (Peng et al. 2021c)**. We both show the result from full input (top group) and sparse input (bottom group).

Method:	PSNR $\uparrow$	SSIM $\uparrow$	LPIPS $\downarrow$	FPS
w/o non-rigid	30.32	0.968	30.41	50
w/o contrastive	30.76	0.970	27.58	50
pointnet	30.75	0.970	27.74	50
w/o DAA	30.78	0.970	27.83	50
Full model	30.81	0.970	27.48	50
w/o con	30.33	0.968	29.96	50
w/o DAA	30.42	0.968	30.17	50
Full model	30.41	0.969	29.94	50

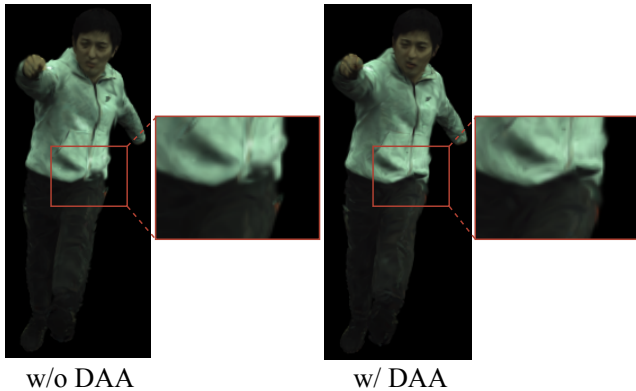


Figure 4: **Ablation Study** on Dynamic Avatar Adjustment, which enhances multi-view consistency, hence improving rendering quality.

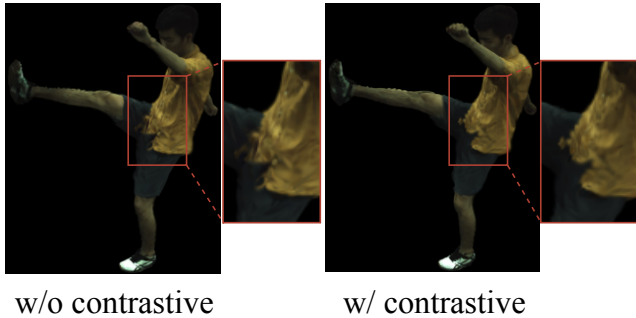


Figure 5: **Ablation Study** on 3D geometry contrastive learning, which removes the artifacts on highly articulated poses..

### Ablation Study

In this section, we conduct ablation experiments using the ZJU-MoCap (Peng et al. 2021c) dataset with both full inputs and sparse inputs to evaluate the effectiveness of our proposed modules. We also conduct experiments to evaluate different backbones in 3D geometry contrastive learning. **Notably, our CHASE maintains 3D consistency effectively without increasing any extra inference time.**

**Non-rigid Deformation.** Non-rigid Deformation is designed for complex cloth deformation. As shown in Tab. 3, non-rigid deformation is required to achieve optimal performance, demonstrating non-rigid regions are well rendered.

**Dynamic Avatar Adjustment.** As shown in Tab.3, incorporating Dynamic Avatar Adjustment (DAA) results in our full model outperforming the baseline in terms of LPIPS. **We argue that LPIPS is particularly informative compared to other metrics because it addresses the challenge of accurately reproducing ground-truth appearance from novel views in a monocular setting**(Qian et al. 2024; Yang et al. 2024). Fig. 4 illustrates that Dynamic Avatar Adjustment serves as an effective 2D image supervision technique for 3D human body modeling, enhancing 3D consistency and reducing artifacts while improving multi-view consistency.

**3D geometry contrastive learning.** Our core idea is that cross-3D-modal contrastive learning can facilitate communication between 3D models for obtaining powerful representations. To verify this, we further do ablation studies to show qualitative comparisons in Tab. 3 and Fig. 5. We can find the full model (w/ contrastive) preserves finer details and provides a more realistic and detailed reconstruction of clothing and other complex surfaces, demonstrating that 3D Geometry Contrastive Learning enhances 3D consistency.

**Backbone for 3D contrastive learning.** In Tab. 3, We show the ablation study on different backbones, including PointNet (Qi et al. 2017) (pointnet) and DGCNN (Wang et al. 2019) (full model). This indicates that DGCNN captures local geometric details better by building a dynamic graph structure, while PointNet relies on global feature learning, which may cause some local information to be missing.

### Conclusion

In this paper, we present **CHASE**, a 3D-consistent human modeling framework utilizing Gaussian Splatting with both full and sparse inputs. We first integrates a skeleton-driven rigid deformation and a non-rigid cloth dynamics deformation to create human avatar. To improve 3D consistency under sparse inputs, we use the intrinsic 3D consistency of images across poses. For each training image, we select similar pose/image from the dataset and adjust the deformed Gaussians to selected pose by Dynamic Avatar Adjustment (DAA). Minimizing the difference between the image rendered by adjusted Gaussians and image paired with selected similar pose serves as an additional supervision, hence enhancing the 3D consistency of human avatars. Furthermore, to enforce global 3D consistency across different representations of the same pose, we propose a 3D geometry contrastive learning. Extensive experiments on two popular datasets demonstrate that **CHASE** not only achieves superior fidelity in generating human avatars compared to current SOTA methods but also excels in handling both monocular and sparse input scenarios. We hope that our method could foster further research in high-quality clothed human avatar synthesis from monocular views.

**Limitations.** 1). **CHASE** lacks the capability to extract 3D meshes. Developing a method to extract meshes from 3D

Gaussians is an important direction for future research. 2). Our **CHASE** need to find similar pose from dataset. When it comes to monocular videos featuring large-scale movements and diverse actions, it is hard to find pairs that qualify the requirements, which may impact performance.

## References

- Afham, M.; Dissanayake, I.; Dissanayake, D.; Dharmasiri, A.; Thilakarathna, K.; and Rodrigo, R. 2022. Cross-point: Self-supervised cross-modal contrastive learning for 3d point cloud understanding. In *Proc. of IEEE Conf. on Computer Vision and Pattern Recognition*, 9902–9912.
- Chen, M.; Zhang, J.; Xu, X.; Liu, L.; Cai, Y.; Feng, J.; and Yan, S. 2022. Geometry-guided progressive nerf for generalizable and efficient neural human rendering. In *Proc. of European Conf. on Computer Vision*, 222–239.
- Chen, Y.; Chen, Z.; Zhang, C.; Wang, F.; Yang, X.; Wang, Y.; Cai, Z.; Yang, L.; Liu, H.; and Lin, G. 2024. Gaussianeditor: Swift and controllable 3d editing with gaussian splatting. In *Proc. of IEEE Conf. on Computer Vision and Pattern Recognition*, 21476–21485.
- Gao, L.; Lai, Y.-K.; Yang, J.; Zhang, L.-X.; Xia, S.; and Kobbelt, L. 2019. Sparse data driven mesh deformation. *IEEE transactions on visualization and computer graphics*, 27(3): 2085–2100.
- Guédon, A.; and Lepetit, V. 2024. Sugar: Surface-aligned gaussian splatting for efficient 3d mesh reconstruction and high-quality mesh rendering. In *Proc. of IEEE Conf. on Computer Vision and Pattern Recognition*, 5354–5363.
- Hadsell, R.; Chopra, S.; and LeCun, Y. 2006. Dimensionality reduction by learning an invariant mapping. In *Proc. of IEEE Conf. on Computer Vision and Pattern Recognition*, volume 2, 1735–1742.
- Healey, J.; Wang, J.; and et al. 2021. A mixed-reality system to promote child engagement in remote intergenerational storytelling. In *International Symposium on Mixed and Augmented Reality Adjunct*, 274–279.
- Hu, L.; Zhang, H.; Zhang, Y.; Zhou, B.; Liu, B.; Zhang, S.; and Nie, L. 2024a. Gaussianavatar: Towards realistic human avatar modeling from a single video via animatable 3d gaussians. In *Proc. of IEEE Conf. on Computer Vision and Pattern Recognition*, 634–644.
- Hu, S.; et al. 2024b. GauHuman: Articulated gaussian splatting from monocular human videos. In *cvpr*, 20418–20431.
- Huang, Y.-H.; Sun, Y.-T.; Yang, Z.; Lyu, X.; Cao, Y.-P.; and Qi, X. 2024. SC-GS: Sparse-controlled gaussian splatting for editable dynamic scenes. In *Proc. of IEEE Conf. on Computer Vision and Pattern Recognition*, 4220–4230.
- Ionescu, C.; Papava, D.; Olaru, V.; and Sminchisescu, C. 2013. Human3.6m: Large scale datasets and predictive methods for 3d human sensing in natural environments. *IEEE Trans. on Pattern Anal. and Mach. Intell.*, 36(7): 1325–1339.
- Jiang, T.; Chen, X.; Song, J.; and Hilliges, O. 2023. InstantAvatar: Learning Avatars from Monocular Video in 60 Seconds. In *Proc. of IEEE Conf. on Computer Vision and Pattern Recognition*, 16922–16932.
- Kerbl, B.; Kopanas, G.; Leimkühler, T.; and Drettakis, G. 2023. 3d gaussian splatting for real-time radiance field rendering. *ACM Transactions on Graphics*, 42(4): 1–14.
- Khosla, P.; Teterwak, P.; Wang, C.; Sarna, A.; Tian, Y.; Isola, P.; Maschinot, A.; Liu, C.; and Krishnan, D. 2020. Supervised contrastive learning. *Proc. of Advances in Neural Information Processing Systems*, 33: 18661–18673.
- Kocabas, M.; Chang, J.-H. R.; Gabriel, J.; Tuzel, O.; and Ranjan, A. 2024. HUGS: Human gaussian splats. In *Proc. of IEEE Conf. on Computer Vision and Pattern Recognition*, 505–515.
- Kwon, Y.; Fang, B.; Lu, Y.; Dong, H.; Zhang, C.; Carrasco, F. V.; Mosella-Montoro, A.; Xu, J.; Takagi, S.; Kim, D.; et al. 2024. Generalizable Human Gaussians for Sparse View Synthesis. *arXiv preprint arXiv:2407.12777*.
- Lei, J.; Wang, Y.; Pavlakos, G.; Liu, L.; and Daniilidis, K. 2024. GART: Gaussian articulated template models. In *Proc. of IEEE Conf. on Computer Vision and Pattern Recognition*, 19876–19887.
- Li, Z.; Zheng, Z.; Liu, Y.; Zhou, B.; and Liu, Y. 2023. Posevocab: Learning joint-structured pose embeddings for human avatar modeling. In *ACM SIGGRAPH 2023 Conference Proceedings*, 1–11.
- Liu, L.; Habermann, M.; Rudnev, V.; Sarkar, K.; Gu, J.; and Theobalt, C. 2021. Neural actor: Neural free-view synthesis of human actors with pose control. *ACM transactions on graphics (TOG)*, 40(6): 1–16.
- Loper, M.; Mahmood, N.; Romero, J.; Pons-Moll, G.; and Black, M. J. 2015. SMPL: A Skinned Multi-Person Linear Model. *Acm Transactions on Graphics*, 34(248).
- Mihajlovic, M.; Zhang, Y.; Black, M. J.; and Tang, S. 2021. LEAP: Learning articulated occupancy of people. In *Proc. of IEEE Conf. on Computer Vision and Pattern Recognition*, 10461–10471.
- Mildenhall, B.; Srinivasan, P. P.; Tancik, M.; Barron, J. T.; Ramamoorthi, R.; and Ng, R. 2021. Nerf: Representing scenes as neural radiance fields for view synthesis. *Communications of the ACM*, 65(1): 99–106.
- Moreau, A.; Song, J.; Dhano, H.; Shaw, R.; Zhou, Y.; and Pérez-Pellitero, E. 2024. Human gaussian splatting: Real-time rendering of animatable avatars. In *Proc. of IEEE Conf. on Computer Vision and Pattern Recognition*, 788–798.
- Niemeyer, M.; Mescheder, L.; Oechsle, M.; and Geiger, A. 2020. Differentiable volumetric rendering: Learning implicit 3d representations without 3d supervision. In *Proc. of IEEE Conf. on Computer Vision and Pattern Recognition*, 3504–3515.
- Noguchi, A.; Sun, X.; Lin, S.; and Harada, T. 2021. Neural articulated radiance field. In *Proc. of IEEE Intl. Conf. on Computer Vision*, 5762–5772.
- Oechsle, M.; Peng, S.; and Geiger, A. 2021. Unisurf: Unifying neural implicit surfaces and radiance fields for multi-view reconstruction. In *Proc. of IEEE Intl. Conf. on Computer Vision*, 5589–5599.
- Peng, S.; Dong, J.; Wang, Q.; Zhang, S.; Shuai, Q.; Zhou, X.; and Bao, H. 2021a. Animatable neural radiance fields



- for modeling dynamic human bodies. In *Proc. of IEEE Intl. Conf. on Computer Vision*, 14314–14323.
- Peng, S.; Jiang, C.; Liao, Y.; Niemeyer, M.; Pollefeys, M.; and Geiger, A. 2021b. Shape as points: A differentiable poisson solver. *Proc. of Advances in Neural Information Processing Systems*, 34: 13032–13044.
- Peng, S.; Zhang, Y.; Xu, Y.; Wang, Q.; Shuai, Q.; Bao, H.; and Zhou, X. 2021c. Neural Body: Implicit Neural Representations with Structured Latent Codes for Novel View Synthesis of Dynamic Humans. In *Proc. of IEEE Conf. on Computer Vision and Pattern Recognition*, 9054–9063.
- Qi, C. R.; Su, H.; Mo, K.; and Guibas, L. J. 2017. Pointnet: Deep learning on point sets for 3d classification and segmentation. In *Proc. of IEEE Conf. on Computer Vision and Pattern Recognition*, 652–660.
- Qi, Z.; Dong, R.; Fan, G.; Ge, Z.; Zhang, X.; Ma, K.; and Yi, L. 2023. Contrast with reconstruct: Contrastive 3d representation learning guided by generative pretraining. In *Proc. of Intl. Conf. on Machine Learning*, 28223–28243.
- Qian, Z.; Wang, S.; Mihajlovic, M.; Geiger, A.; and Tang, S. 2024. 3dgs-avatar: Animatable avatars via deformable 3d gaussian splatting. In *Proc. of IEEE Conf. on Computer Vision and Pattern Recognition*, 5020–5030.
- Radford, A.; Kim, J. W.; Hallacy, C.; Ramesh, A.; Goh, G.; Agarwal, S.; Sastry, G.; Askell, A.; Mishkin, P.; Clark, J.; et al. 2021. Learning transferable visual models from natural language supervision. In *Proc. of Intl. Conf. on Machine Learning*, 8748–8763.
- Rumen, D.; Li, J.; Charlotte, L.; Seungwook, H.; Akash, S.; Brian, C.; Pulkit, A.; and Marin, S. 2022. Equivariant self-supervised learning: Encouraging equivariance in representations. In *Proc. of International Conference on Learning Representations*.
- Shao, Z.; Wang, Z.; Li, Z.; Wang, D.; Lin, X.; Zhang, Y.; Fan, M.; and Wang, Z. 2024. SplattingAvatar: Realistic real-time human avatars with mesh-embedded gaussian splatting. In *Proc. of IEEE Conf. on Computer Vision and Pattern Recognition*, 1606–1616.
- Sitzmann, V.; Rezkikov, S.; Freeman, B.; Tenenbaum, J.; and Durand, F. 2021. Light field networks: Neural scene representations with single-evaluation rendering. *Proc. of Advances in Neural Information Processing Systems*, 34: 19313–19325.
- Sorkine, O. 2005. Laplacian mesh processing. *Eurographics (State of the Art Reports)*, 4(4): 1.
- Sorkine, O.; and Alexa, M. 2007. As-rigid-as-possible surface modeling. In *Symposium on Geometry processing*, volume 4, 109–116.
- Sumner, R. W.; Schmid, J.; and Pauly, M. 2007. Embedded deformation for shape manipulation. In *ACM siggraph 2007 papers*, 80–es.
- Wang, H.; Ren, J.; Huang, Z.; Olszewski, K.; Chai, M.; Fu, Y.; and Tulyakov, S. 2022a. R2l: Distilling neural radiance field to neural light field for efficient novel view synthesis. In *Proc. of European Conf. on Computer Vision*, 612–629. Springer.
- Wang, H.; Zhang, W.; Liu, S.; Zhou, X.; Zhang, S.; Wu, F.; and Lin, F. 2024a. Gaussian Control with Hierarchical Semantic Graphs in 3D Human Recovery. *arXiv preprint arXiv:2405.12477*.
- Wang, S.; Schwarz, K.; Geiger, A.; and Tang, S. 2022b. ARAH: Animatable Volume Rendering of Articulated Human SDFs. In *Proc. of European Conf. on Computer Vision*, 1–19.
- Wang, Y.; Sun, Y.; Liu, Z.; Sarma, S. E.; Bronstein, M. M.; and Solomon, J. M. 2019. Dynamic graph cnn for learning on point clouds. *ACM Transactions on Graphics (tog)*, 38(5): 1–12.
- Wang, Y.; Yi, X.; Wu, Z.; Zhao, N.; Chen, L.; and Zhang, H. 2024b. View-consistent 3d editing with gaussian splatting. *arXiv preprint arXiv:2403.11868*.
- Wen, J.; Zhao, X.; Ren, Z.; Schwing, A. G.; and Wang, S. 2024. GomavAtar: Efficient animatable human modeling from monocular video using gaussians-on-mesh. In *Proceedings of the IEEE/CVF Conference on Computer Vision and Pattern Recognition*, 2059–2069.
- Weng, C.-Y.; Curless, B.; Srinivasan, P. P.; Barron, J. T.; and Kemelmacher-Shlizerman, I. 2022. HumanNeRF: Free-viewpoint Rendering of Moving People from Monocular Video. In *Proc. of IEEE Conf. on Computer Vision and Pattern Recognition*, 16210–16220.
- Xie, S.; Gu, J.; Guo, D.; Qi, C. R.; Guibas, L.; and Litany, O. 2020. Pointcontrast: Unsupervised pre-training for 3d point cloud understanding. In *Proc. of European Conf. on Computer Vision*, 574–591.
- Yang, C.; Li, S.; Fang, J.; Liang, R.; Xie, L.; Zhang, X.; Shen, W.; and Tian, Q. 2024. Gaussianobject: Just taking four images to get a high-quality 3d object with gaussian splatting. *arXiv preprint arXiv:2402.10259*.
- Yifan, W.; Aigerman, N.; Kim, V. G.; Chaudhuri, S.; and Sorkine-Hornung, O. 2020. Neural cages for detail-preserving 3d deformations. In *Proc. of IEEE Conf. on Computer Vision and Pattern Recognition*, 75–83.
- Yifan, W.; Serena, F.; Wu, S.; Öztireli, C.; and Sorkine-Hornung, O. 2019. Differentiable surface splatting for point-based geometry processing. *ACM Transactions on Graphics*, 38(6): 1–14.
- Yu, Y.; Zhou, K.; Xu, D.; Shi, X.; Bao, H.; Guo, B.; and Shum, H.-Y. 2004. Mesh editing with poisson-based gradient field manipulation. In *ACM SIGGRAPH*, 644–651.
- Yu, Z.; Cheng, W.; Liu, x.; Wu, W.; and Lin, K.-Y. 2023. MonoHuman: Animatable Human Neural Field from Monocular Video. In *Proc. of IEEE Conf. on Computer Vision and Pattern Recognition*, 16943–16953.
- Zackariasson, P.; and Wilson, T. L. 2012. The video game industry: Formation, present state, and future.
- Zhang, R.; Guo, Z.; Zhang, W.; Li, K.; Miao, X.; Cui, B.; Qiao, Y.; Gao, P.; and Li, H. 2022. Pointclip: Point cloud understanding by clip. In *Proc. of IEEE Conf. on Computer Vision and Pattern Recognition*, 8552–8562.
- Zhao, F.; Yang, W.; Zhang, J.; Lin, P.; Zhang, Y.; Yu, J.; and Xu, L. 2022. Humannerf: Efficiently generated human

radiance field from sparse inputs. In *Proc. of IEEE Conf. on Computer Vision and Pattern Recognition*, 7743–7753.

Zheng, Y.; Yifan, W.; Wetzstein, G.; Black, M. J.; and Hilliges, O. 2023. Pointavatar: Deformable point-based head avatars from videos. In *Proc. of IEEE Conf. on Computer Vision and Pattern Recognition*, 21057–21067.

## Reproducibility Checklist

This paper:

- Includes a conceptual outline and/or pseudocode description of AI methods introduced. (yes)
- Clearly delineates statements that are opinions, hypothesis, and speculation from objective facts and results. (yes)
- Provides well marked pedagogical references for less-familare readers to gain background necessary to replicate the paper. (yes)

Does this paper make theoretical contributions? (yes)

- All assumptions and restrictions are stated clearly and formally. (yes)
- All novel claims are stated formally (e.g., in theorem statements). (yes)
- Proofs of all novel claims are included. (yes)
- Proof sketches or intuitions are given for complex and/or novel results. (yes)
- Appropriate citations to theoretical tools used are given. (yes)
- All theoretical claims are demonstrated empirically to hold. (yes)
- All experimental code used to eliminate or disprove claims is included. (NA)

Does this paper rely on one or more datasets? (yes)

- A motivation is given for why the experiments are conducted on the selected datasets. (yes)
- All novel datasets introduced in this paper are included in a data appendix. (NA)
- All novel datasets introduced in this paper will be made publicly available upon publication of the paper with a license that allows free usage for research purposes. (NA)
- All datasets drawn from the existing literature (potentially including authors' own previously published work) are accompanied by appropriate citations. (yes)
- All datasets drawn from the existing literature (potentially including authors' own previously published work) are publicly available. (yes)
- All datasets that are not publicly available are described in detail, with explanation why publicly available alternatives are not scientifically satisficing. (yes)

Does this paper include computational experiments? (yes)

- Any code required for pre-processing data is included in the appendix. (yes)
- All source code required for conducting and analyzing the experiments is included in a code appendix. (no) Our code will be made available upon publication of the article.

- All source code required for conducting and analyzing the experiments will be made publicly available upon publication of the paper with a license that allows free usage for research purposes. (yes)
- All source code implementing new methods have comments detailing the implementation, with references to the paper where each step comes from. (yes)
- If an algorithm depends on randomness, then the method used for setting seeds is described in a way sufficient to allow replication of results. (yes)
- This paper specifies the computing infrastructure used for running experiments (hardware and software), including GPU/CPU models; amount of memory; operating system; names and versions of relevant software libraries and frameworks. (yes)
- This paper formally describes evaluation metrics used and explains the motivation for choosing these metrics. (yes)
- This paper states the number of algorithm runs used to compute each reported result. (yes)
- Analysis of experiments goes beyond single-dimensional summaries of performance (e.g., average; median) to include measures of variation, confidence, or other distributional information. (yes)
- The significance of any improvement or decrease in performance is judged using appropriate statistical tests (e.g., Wilcoxon signed-rank). (yes)
- This paper lists all final (hyper-)parameters used for each model/algorithm in the paper's experiments. (yes)
- This paper states the number and range of values tried per (hyper-) parameter during development of the paper, along with the criterion used for selecting the final parameter setting. (yes)

## Implementation Details

We preprocess the dataset following the ARAH<sup>1</sup>. During optimization, we follow the same strategy from (Kerbl et al. 2023) to densify and prune the 3D Gaussians, using the view-space position gradients derived from the transformed Gaussians in the observation space as the criterion for densification.

The similar pose/image is selected by computing the orientation and limb angle difference provided by smpl model. For each pose/image, we select at most 3 similar poses/images.

Our model is trained for a total of  $13k$  iterations on the ZJU-MoCap (Peng et al. 2021c) dataset and  $10k$  iterations on H36M (Ionescu et al. 2013) on a single NVIDIA RTX 3090 GPU. We use Adam to optimize our model and the per-frame latent codes with hyperparameters  $\beta_1 = 0.9$  and  $\beta_2 = 0.999$ . The learning rate of 3D Gaussians is exactly the same as the original implementation from (Kerbl et al. 2023). We set the learning rate for forward skinning network  $\theta_r$  to  $1 \times 10^{-4}$ ,  $1 \times 10^{-4}$  for DGCNN and MLP in point cloud encoder, and  $1 \times 10^{-3}$  for all the others. An exponential learning rate scheduler is employed to gradually decrease the learning rate by a factor of 0.1 on neural networks. We also apply a weight decay with a weight of 0.05 to the per-frame latent codes.

Following prior works (Weng et al. 2022; Qian et al. 2024), we split the training stage and learn the whole model in a coarse-to-fine manner. In the first  $1k$  iterations, we freeze everything except the forward skinning network  $f_{\theta_r}$  to learn a coarse skinning field with  $\mathcal{L}_{skin}$ . We then enable optimization on the 3D Gaussians after  $1k$  steps. To decouple rigid and non-rigid motion, we start to optimize the non-rigid deformation network  $f_{\theta_{nr}}$  after  $3k$  iterations. Lastly, we turn on Geometric and Semantic Feature Learning after  $5k$  iterations.

## Implementation Details for Baselines

In this section, we elaborate on the implementation details of baselines used for comparison to our proposed method, *i.e.* NeuralBody (Peng et al. 2021c), HumanNeRF (Weng et al. 2022), MonoHuman (Yu et al. 2023) and InstantAvatar (Jiang et al. 2023).

For NeuralBody (Peng et al. 2021c), HumanNeRF (Weng et al. 2022), MonoHuman (Yu et al. 2023) and InstantAvatar (Jiang et al. 2023), we use the results of them reported in 3DGS-Avatar (Qian et al. 2024) which follow the same data split.

For 3DGS-Avatar (Qian et al. 2024), we train the models using the code from official code repository<sup>2</sup>. For GauHuman (Hu et al. 2024b), we train the models using the code from official code repository<sup>3</sup> for 15000 epochs. For GoMAvatar (Wen et al. 2024), we train the models using the code from official code repository<sup>4</sup>. All other hyperparameters re-

main unchanged. The trained models are then used for qualitative evaluation and out-of-distribution pose animation.

## Loss Definition

In the main paper we describe our loss term which can be formulated as follows:

$$\mathcal{L}_{rgb} = (1 - \lambda_{adjust})\mathcal{L}_{rgb}^o + \lambda_{adjust}\mathcal{L}_{rgb}^a, \quad (17)$$

$$\mathcal{L}_{mask} = (1 - \lambda_{adjust})\mathcal{L}_{mask}^o + \lambda_{adjust}\mathcal{L}_{mask}^a, \quad (18)$$

$$\mathcal{L}_{LPIPS} = (1 - \lambda_{adjust})\mathcal{L}_{LPIPS}^o + \lambda_{adjust}\mathcal{L}_{LPIPS}^a, \quad (19)$$

$$\mathcal{L}_{skin} = (1 - \lambda_{adjust})\mathcal{L}_{skin}^o + \lambda_{adjust}\mathcal{L}_{skin}^a, \quad (20)$$

$$\mathcal{L}_{isopos} = (1 - \lambda_{adjust})\mathcal{L}_{isopos}^o + \lambda_{adjust}\mathcal{L}_{isopos}^a, \quad (21)$$

$$\mathcal{L}_{isocov} = (1 - \lambda_{adjust})\mathcal{L}_{isocov}^o + \lambda_{adjust}\mathcal{L}_{isocov}^a, \quad (22)$$

where  $\mathcal{L}_{rgb}^o, \mathcal{L}_{mask}^o, \mathcal{L}_{LPIPS}^o, \mathcal{L}_{skin}^o, \mathcal{L}_{isopos}^o, \mathcal{L}_{isocov}^o$  are the losses on images rendered from the deformed Gaussians  $\mathcal{G}_o$ , while  $\mathcal{L}_{rgb}^a, \mathcal{L}_{mask}^a, \mathcal{L}_{LPIPS}^a, \mathcal{L}_{skin}^a, \mathcal{L}_{isopos}^a, \mathcal{L}_{isocov}^a$  are the losses on images rendered from the adjusted Gaussians  $\mathcal{G}_a$ . We set  $\lambda_{adjust}$  as 0.1 in this function. We describe how each loss term is defined below:

**RGB Loss.** We employ an  $l1$  loss for pixel-wise error and a perceptual loss for robustness against local misalignments, crucial in monocular setups.

**Mask Loss.** To boost the convergence of 3D Gaussian positions, we use an explicit mask loss. For each pixel  $p$ , we compute the opacity value  $O_p$  by summing up the sample weights in the rendering equation in the main paper:

$$O_p = \sum_i \alpha'_i \prod_{j=1}^{i-1} (1 - \alpha'_j). \quad (23)$$

We thus supervise it with the ground truth foreground mask via an  $l1$  loss. Experiments show that the  $l1$  loss provides faster convergence than the Binary Cross Entropy (BCE) loss.

**LPIPS Loss.** Following (Weng et al. 2022), we use VGG-based LPIPS as the perceptual loss. Unlike NeRF methods, we render full images via rasterization, eliminating the need for patch sampling. For efficiency, we compute LPIPS on cropped bounding boxes using ground truth masks:

$$\mathcal{L}_{LPIPS} = LPIPS(\hat{C}, C). \quad (24)$$

**Skinning Loss:** We leverage SMPL prior by sampling 1024 points  $\mathbf{X}_{skin}$  on the surface of the canonical SMPL mesh and regularizing the forward skinning network with corresponding skinning weights  $\mathbf{w}$  interpolated with barycentric coordinates.

$$\mathcal{L}_{skin} = \frac{1}{|\mathbf{X}_{skin}|} \sum_{\mathbf{x}_{skin} \in \mathbf{X}_{skin}} \|f_{\theta_r}(\mathbf{x}_{skin}) - \mathbf{w}\|^2. \quad (25)$$

<sup>1</sup><https://github.com/taconite/arah-release>

<sup>2</sup><https://github.com/mikeqzy/3dgs-avatar-release>

<sup>3</sup><https://github.com/skhu101/GauHuman>

<sup>4</sup><https://github.com/wenj/GoMAvatar>

In  $\mathcal{L}_o'$ , target images are the similar images selected from the dataset and synthesized images rendered from adjusted  $\mathcal{G}_a$ . We set  $\lambda_1 = 0.1, \lambda_2 = 0.01, \lambda_3 = 0.1, \lambda_4 = 1, \lambda_5 = 100, \lambda_6 = 0.001$  in all experiments. For  $\lambda_3$ , we set it to 10 for the first  $1k$  iterations for fast convergence to a reasonable skinning field, then decreased to 0.1 for soft regularization. For  $\lambda_{adjust}$  and  $\lambda_6$  we set them to 0 until 8k iterations. We also set  $\lambda_{adjust}$  to 0.001 after 9k iterations.

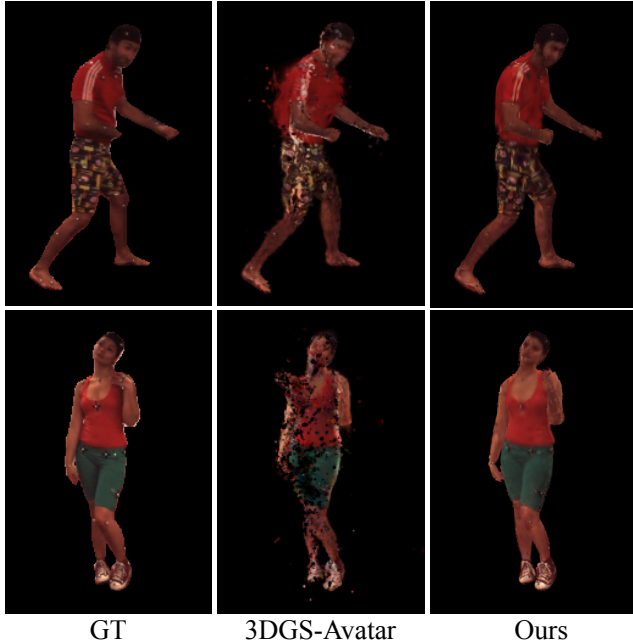


Figure 6: **Qualitative Comparison on H36M (Ionescu et al. 2013) with sparse inputs.** We demonstrate that our method, CHASE, effectively produces realistic details for novel pose in both rendered images and geometry, whereas other approaches struggle to achieve smooth details.

### Novel Pose Renderings

For qualitative comparisons on novel pose synthesis, as shown in Fig 6, our method generalizes well to novel pose with just sparse inputs (only 5% of origin data) and reconstruct human avatars with better appearance and geometry detail.

### Reproducibility Checklist

This paper:

- Includes a conceptual outline and/or pseudocode description of AI methods introduced. (yes)
- Clearly delineates statements that are opinions, hypothesis, and speculation from objective facts and results. (yes)
- Provides well marked pedagogical references for less-familiar readers to gain background necessary to replicate the paper. (yes)

Does this paper make theoretical contributions? (yes)

- All assumptions and restrictions are stated clearly and formally. (yes)
- All novel claims are stated formally (e.g., in theorem statements). (yes)
- Proofs of all novel claims are included. (yes)
- Proof sketches or intuitions are given for complex and/or novel results. (yes)
- Appropriate citations to theoretical tools used are given. (yes)
- All theoretical claims are demonstrated empirically to hold. (yes)
- All experimental code used to eliminate or disprove claims is included. (NA)

Does this paper rely on one or more datasets? (yes)

- A motivation is given for why the experiments are conducted on the selected datasets. (yes)
- All novel datasets introduced in this paper are included in a data appendix. (NA)
- All novel datasets introduced in this paper will be made publicly available upon publication of the paper with a license that allows free usage for research purposes. (NA)
- All datasets drawn from the existing literature (potentially including authors' own previously published work) are accompanied by appropriate citations. (yes)
- All datasets drawn from the existing literature (potentially including authors' own previously published work) are publicly available. (yes)
- All datasets that are not publicly available are described in detail, with explanation why publicly available alternatives are not scientifically satisfying. (yes)

Does this paper include computational experiments? (yes)

- Any code required for pre-processing data is included in the appendix. (yes)
- All source code required for conducting and analyzing the experiments is included in a code appendix. (no) Our code will be made available upon publication of the article.
- All source code required for conducting and analyzing the experiments will be made publicly available upon publication of the paper with a license that allows free usage for research purposes. (yes)
- All source code implementing new methods have comments detailing the implementation, with references to the paper where each step comes from. (yes)
- If an algorithm depends on randomness, then the method used for setting seeds is described in a way sufficient to allow replication of results. (yes)
- This paper specifies the computing infrastructure used for running experiments (hardware and software), including GPU/CPU models; amount of memory; operating system; names and versions of relevant software libraries and frameworks. (yes)
- This paper formally describes evaluation metrics used and explains the motivation for choosing these metrics. (yes)

- This paper states the number of algorithm runs used to compute each reported result. (yes)
- Analysis of experiments goes beyond single-dimensional summaries of performance (e.g., average; median) to include measures of variation, confidence, or other distributional information. (yes)
- The significance of any improvement or decrease in performance is judged using appropriate statistical tests (e.g., Wilcoxon signed-rank). (yes)
- This paper lists all final (hyper-)parameters used for each model/algorithm in the paper's experiments. (yes)
- This paper states the number and range of values tried per (hyper-) parameter during development of the paper, along with the criterion used for selecting the final parameter setting. (yes)